JACS
JOURNAL OF THE AMERICAN CHEMICAL SOCIETY
Article
pubs.acs.org/JACS

Chiral NH-Controlled Supramolecular Metallacycles

Jinqiao Dong,[†] Chunxia Tan,[†] Kang Zhang,[‡] Yan Liu,[*,†] Paul J. Low,[¶] Jianwen Jiang,[‡] and Yong Cui[*,†,⊥]

[†]School of Chemistry and Chemical Technology and State Key Laboratory of Metal Matrix Composites, Shanghai Jiao Tong University, Shanghai 200240, China

[‡]Department of Chemical and Biomolecular Engineering, National University of Singapore, 4 Engineering Drive 4, 117576 Singapore

[¶]School of Chemistry and Biochemistry, University of Western Australia, 35 Stirling Highway, Crawley, WA 6009, Australia

[⊥]Collaborative Innovation Center of Chemical Science and Engineering, Tianjin 300072, China

Supporting Information

ABSTRACT: Chiral NH functionalities-based discrimination is a key feature of Nature's chemical armory, yet selective binding of biologically active molecules in synthetic systems with high enantioselectivity poses significant challenges. Here we report the assembly of three chiral fluorescent Zn_6L_6 metallacycles from pyridyl-functionalized Zn(salalen) or Zn(salen) complexes. Each of these metallacycles has a nanoscale hydrophobic cavity decorated with six, three, or zero chiral NH functionalities and packs into a three-dimensional supramolecular porous framework. The binding affinity and enantioselectivity of the metallacycles toward α-hydroxycarboxylic acids, amino acids, small molecule pharamaceuticals (L-dopa, D-penicillamine), and chiral amines increase with the number of chiral NH moieties in the cyclic structure. From single-crystal X-ray diffraction, molecular simulations, and quantum chemical calculations, the chiral recognition and discrimination are attributed to the specific binding of enantiomers in the chiral pockets of the metallacycles. The parent metallacycles are fluorescent with the intensity of emission being linearly related to the enantiomeric composition of the chiral biorelevant guests, which allow them to be utilized in chiral sensing. The fact that manipulation of chiral NH functionalities in metallacycles can control the enantiorecognition of biomolecular complexes would facilitate the design of more effective supramolecular assemblies for enantioselective processes.

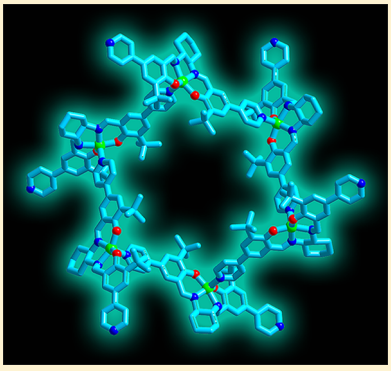

INTRODUCTION

We live in a chiral world. Nature exhibits a remarkable degree of specificity in the chiral recognition of biomolecules, leading to the mirror image arrangements of the two forms eliciting quite different biological responses.[1] In particular, chiral NH functionalities have played a key role in the origin of homochirality in living systems such as DNA, RNA, peptides, and enzymes.[2] For example, carbohydrate recognition by active enzymes involves a wide range of biological processes, including protein folding and trafficking, cell−cell recognition, and many aspects of immune response.[3] Therefore, the detection and differentiation of biomolecules by NH-based receptors are significant in the fields of synthetic, medicinal, and biological chemistry. Recently, Davis and co-workers successfully realized a series of synthetic supramolecular receptors containing numerous NH functionalities for high-affinity binding of polysaccharides,[4] carbohydrates,[5,6] glucose,[7] and o-glcNAc derivatives.[8] To date, however, only a few reported receptors bearing chiral NH functionalities have been designed to detect and discriminate biological substrates such as carbohydrates, amino acids, amines, and important drug compounds.[9−12] Nevertheless, the development of biomimetic receptors and the understanding of entiorecognition mechanisms with well-controlled chiral NH functionalities have not yet been achieved.

Nature's chiroselective phenomena have motivated the quest for synthetic materials with enantioselective capability. Interestingly, chiral supramolecular coordination complexes (SCCs), similar structures to many functional enzymes in living organs, can be constructed by spontaneous coordination-driven self-assembly,[13−16] thereby leading to a large number of molecular architectures, including discrete chiral metallacycles with well-defined internal cavities with size, shape, and functional tunability. This provides the impetus for applications in enantioselective separation,[17−19] catalysis,[20−22] and molecular recognition.[11,12,15] Among them, light-emitting metallacycles have received considerable attention because of their potential applications in chemical sensing and biotechnology.[23] In particular, Stang and co-workers have recently reported tetraphenylethylene (TPE) metallacycles or metallacages with aggregation-induced emission (AIE) behavior for white-light emission,[24] nitroaromatics sensing,[25] anion sensing,[26] and turn-on fluorescence by tobacco mosaic virus (TMV).[27] However, light-emitting sensor materials based on ultrastable chiral supramolecular metallacycles are relatively underdeveloped despite their prospects as advanced functional porous materials

Received: November 3, 2016
Published: January 6, 2017

© 2017 American Chemical Society

DOI: 10.1021/jacs.6b11422
J. Am. Chem. Soc. 2017, 139, 1554−1564

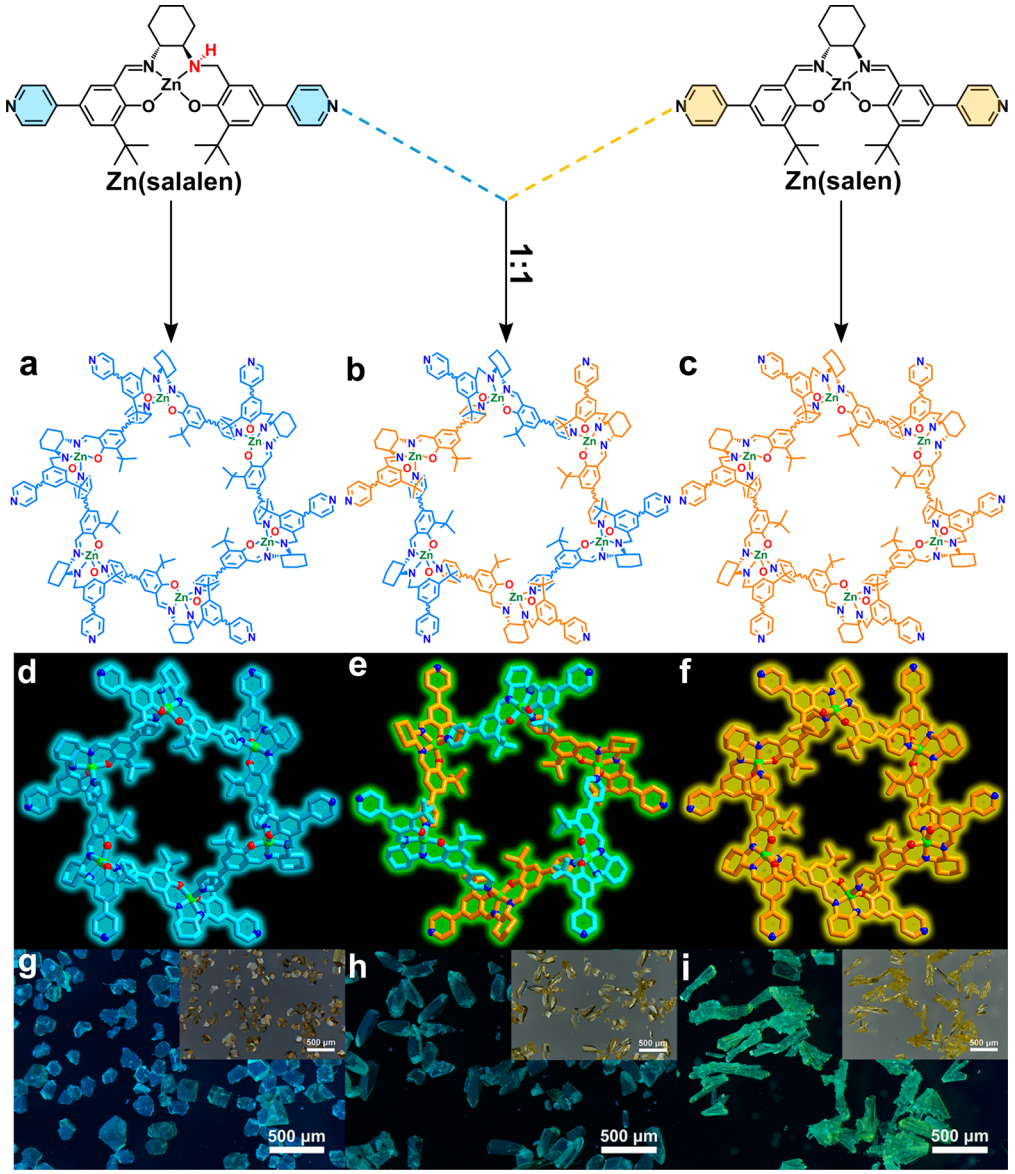

Figure 1. Self-assembly of chiral NH-controlled supramolecular metallacycles (*R*)-**1** (a) from Zn(salalen) and (*R*)-**3** (c) from Zn(salen). (*R*)-**2** (b) was achieved by Zn(salalen) and Zn(salen) with 1:1 ratio. The X-ray crystal structures of chiral metallacycles **1** (d), **2** (e), and **3** (f). Color coding: Zn, green; O, red; N, blue; C atoms of Zn(salalen), cyan; C atoms of Zn(salen), orange. Fluorescent photographs of as-synthesized crystals of (*R*)-**1** (g), (*R*)-**2** (h), and (*R*)-**3** (i) (λ_{ex} = 365 nm; inset: optical photographs).

for chiral liquid or gas sensing.[28] To date, the development of well-controlled and desired chiral NH functionalities in fluorescent metallacycles as biomimetic receptors is still substantially challenging in supramolecular chemistry.[2,14]

To address the issue requires the exploration of new chiral building blocks that can not only provide chiral NH functionalities but also keep high fluorescent emission in metallacycles. As partially reduced analogues of metallosalen complexes, metallosalalen complexes[29] are endowed with higher flexibility and conjugate structures; moreover, the built-in chiral asymmetric NH functionalities would improve its chiral discrimination. Recently, we have reported chiral $Zn_6(salen)_6$ metallacycles assembled from an enantiopure pyridyl-functionalized metallosalen complex.[17] The metallacycle was readily assembled into a tubular supramolecular structure capable of recognizing chiral alcohols but failed to discriminate other important substrates such as sugar acids, amino acids and amino acid-related drugs. With these considerations in mind and inspired by $Zn_6(salen)_6$ synthesis, we envision that the reduction of the salen-based hexamer into salalen-based analogs bearing these additional asymmetric chiral NH functionalities in the cyclic structure may improve its enantioselective discrimination toward a wider range of biorelevant molecular systems. In this article, we report a strategy for the assembly of three chiral NH-controlled supramolecular metallacycles, $Zn_6(salalen)_6$, $Zn_6(salalen)_3(salen)_3$, and $Zn_6(salen)_6$, and demonstrate their use as fluorescent chiral receptors for α-hydroxycarboxylic acids, amino acids, amines, and selected small pharmaceutical molecules, with high binding affinity and enantioselectivity. We directly observe the key role of chiral NH functionalities in the metallacycles that lead to monitoring the chiral recognition and discrimination of biomolecules. X-ray diffraction measurements, molecular simulations, and quantum chemical calculaitons are conducted to provide structural and microscopic insights into the experimentally observed enantiorecognition.

DOI: 10.1021/jacs.6b11422
J. Am. Chem. Soc. 2017, 139, 1554−1564

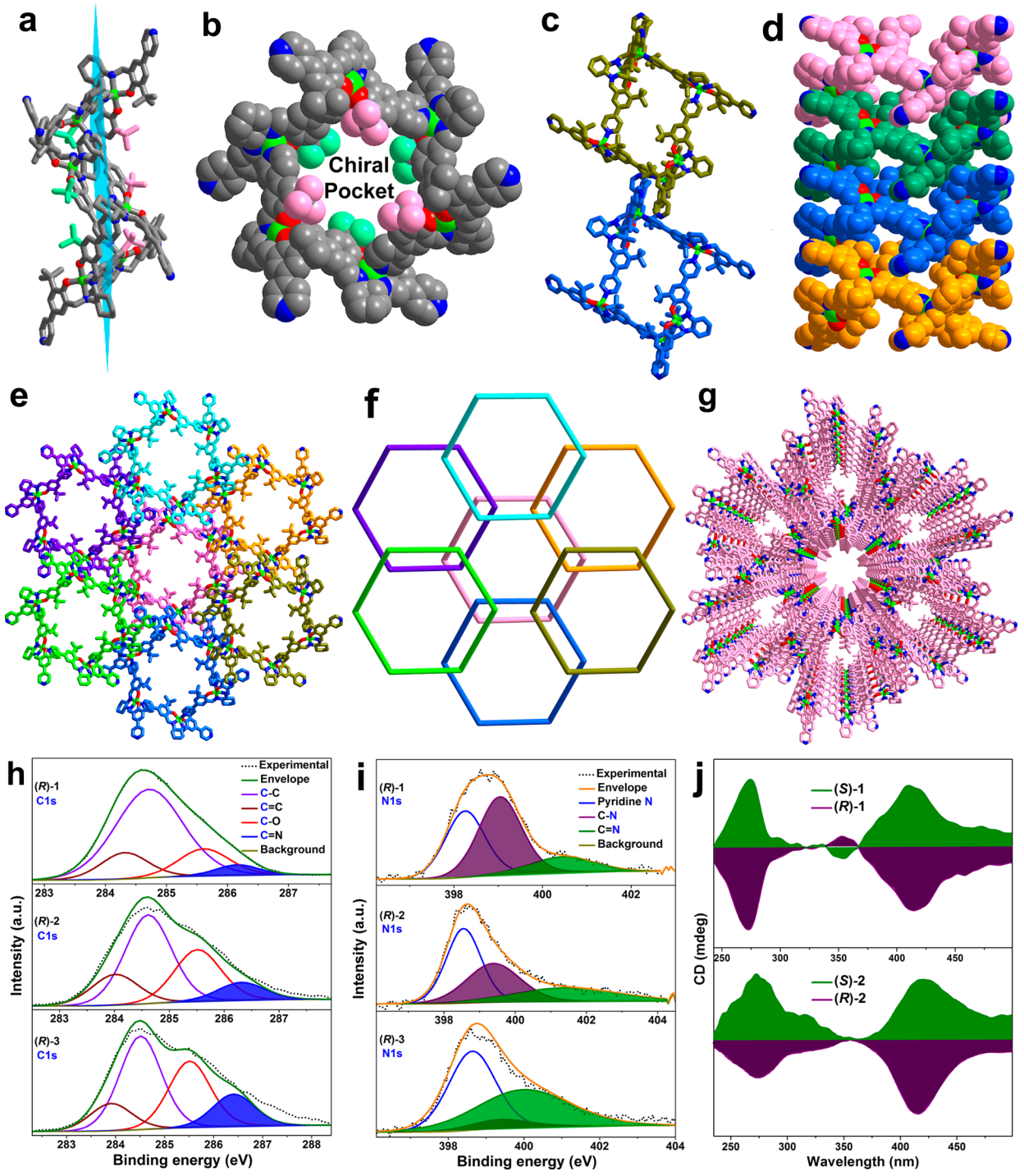

Figure 2. (a) Side-on view of (*R*)-**1**. (b) The top view of six hydrophobic chiral pockets in (*R*)-**1**. (c) Two adjacent metallacycle (*R*)-**1** rings; the rings overlap but do not catenate. (d) Packing of (*R*)-**1** to generate a nanotube along the crystallographic *c*-axis. (e) The extended structures are generated that one ring is shown forming with six other rings through supramolecular interactions. (f) Representation of the connectivity of the arrangement in panel e. (g) Packing of (*R*)-**1** to generate a 3D nanoporous structure viewed along the *c*-axis. Color coding: Zn, green; O, red; N, blue; the different color of C atoms in one ring are shown for clarity. High-resolution C 1s (h) and N 1s (i) XPS spectra of metallacycles **1**−**3**. (j) Solid CD spectra of chiral metallacycle **1** and **2** at room temperature.

RESULTS AND DISCUSSION

Synthesis and Characterization of Chiral NH-Controlled Metallacycles. The salen ligand H_2L^0 and metallacycle **3** ($Zn_6L^0_6$) were prepared as previously reported.[17,30] Herein, the salalen ligand, H_2L^1, was prepared in an overall 79% yield by the Schiff-base condensation of enantiopure 1,2-diaminocyclohexane and 3-*tert*-butyl-5-(4-pyridyl)-salicylaldehyde, followed by reduction with $NaBH_4$ and further condensation with the corresponding salicylaldehyde (Figure S1 and Figure S5). The discrete hexagonal metallacycles $[Zn_6L^1_6]\cdot 8MeOH\cdot 4H_2O$ (**1**) and $[Zn_6L^0_3L^1_3]\cdot 6MeOH\cdot 2H_2O$ (**2**) were obtained by heating $Zn(OAc)_2\cdot 2H_2O$ with H_2L^1 or a mixture of H_2L^0 and H_2L^1 (a 1:1 molar ratio) in DMF and MeOH at 80 °C (Figure 1a−c). Complex **1** containing six free

DOI: 10.1021/jacs.6b11422
J. Am. Chem. Soc. 2017, 139, 1554−1564

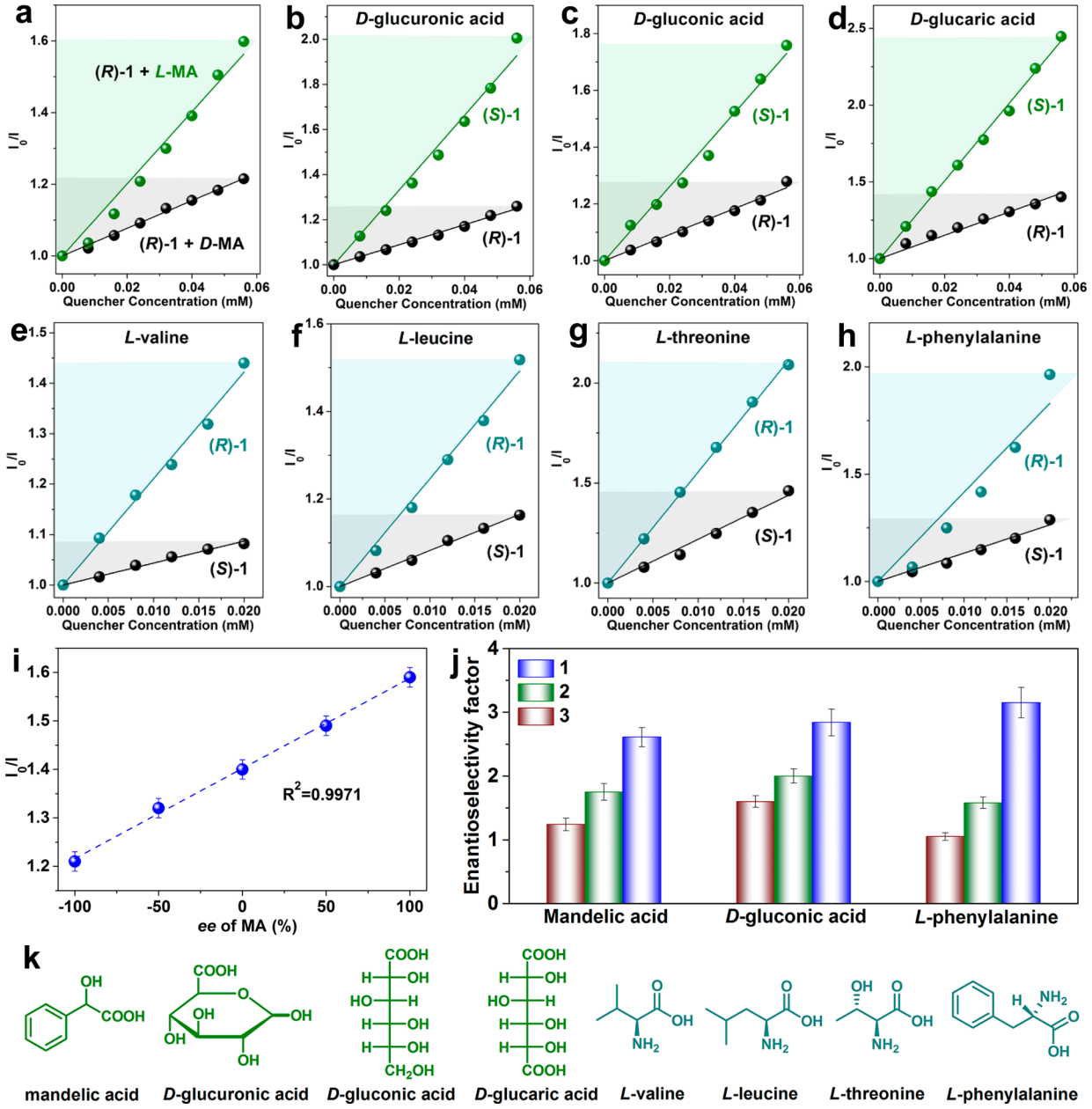

Figure 3. (a) Stern−Völmer plots of (*R*)-**1** titration with L- and D-MA. (b−d) Stern−Völmer plots of (*R*)- and (*S*)-**1** titration with D-glucuronic acid, D-gluconic acid, and D-glucaric acid, respectively. (e−h) Stern−Völmer plots of (*R*)- and (*S*)-**1** titration with L-valine, L-leucine, L-threonine, and L-phenylalanine, respectively. The concentrations of **1** are 2.0×10^{-6} M in THF, and the concentrations of all the acids are 1×10^{-3} M. (i) Plot of I_0/I vs the enantiomeric excess of L-MA at a fixed concentration of 0.56 mM. (j) The compared enantioselectivity factors of chiral metallacycle **1**, **2**, and **3** for mandelic acid, D-gluconic acid, and L-phenylalanine, respectively. (k) The chemical structures of α-hydroxycarboxylic acids and amino acids used in the study.

chiral NH groups emitted cyan fluorescence under UV-light (λ_{ex} = 365 nm), **2** having three chiral NH groups emitted cyan-green fluorescence, whereas **3** with zero NH groups emitted yellow fluorescence (Figure 1g−i). Notably, attempts to prepare salalen-based $Zn_6L^1{}_6$ by direct reduction of the salen-based $Zn_6L^0{}_6$ were unsuccessful. All **1**, **2**, and **3** are sparsely soluble in THF and DMSO (metallacycle **1** is slightly more soluble than the other two) and are insoluble in water and other common organic solvents. Unfortunately, the poor solubility prevented us from obtaining satisfactory ^{1}H NMR spectra of **1**−**3**. The Fourier transform infrared spectroscopy (FT-IR) spectra showed the peaks located at 1590 and 1320 cm^{-1}, which correspond to the C═N vibration and C−N vibration of **1**−**3**, respectively. The difference is that the N−H stretching vibrations were observed in metallacycle **1** and **2** (3420 cm^{-1}) and nonexistent in **3**, indicating the salalen ligand H_2L^1 in the two cyclic structures (Figure S13).

The metallacyclic complexes **1** [$Zn_6L^1{}_6$], **2** [$Zn_6L^0{}_3L^1{}_3$], and **3** [$Zn_6L^0{}_6$] were prepared as shown in Figure 1, with single-crystal X-ray diffraction studies revealing the formation of the isostructural chiral metallacycles (Figure 1d−f). In each case, the Zn centers adopt a distorted square pyramidal geometry with the equatorial plane occupied by the central N_2O_2 donors of one L ligand and the apical position by one pyridine from the imine side arm of another L. Each ZnL unit thus utilizes one pyridyl group to coordinate another Zn atom building a

DOI: 10.1021/jacs.6b11422
J. Am. Chem. Soc. 2017, 139, 1554−1564

hexameric metallacyclic complex with an inner void diameter of 1.2 nm × 1.2 nm and six pendent pyridine moieties decorating the periphery of the cyclic core. The three pairs of *tert*-butyl groups from the ligands L are arranged above and below the metallacyclic cavity (Figure 2a,b). Three kinds of supramolecular interactions direct the packing of **1**−**3** in parallel along the crystallographic *c*-axis into 3D supramolecular porous frameworks without interpenetration (Figure 2c−g): (1) Strong CH···π (2.87−3.10 Å) interactions between the butyl group and the conjugated phenyl ring of adjacent metallacycles along *c*-axis; (2) face-to-face intermolecular $\pi-\pi$ (3.59−3.78 Å) interactions between the adjacent two rings (each Zn_6L_6 unit is engaged in six sets of such $\pi-\pi$ stackings); (3) interlocking of cyclohexyl groups on adjacent metallacycles along *a*-axis and *b*-axis causing strong hydrophobic interactions (Figure S10−S12). The bond lengths of **1** and **2** are typical of salan (C−N, 1.42−1.52 Å) and salen (C═N, 1.23−1.29 Å) structural motifs. In both cases, the NH groups of the L^1 ligands are oriented toward the outside of metallacyclic cavities and exposed to the interstitial pores accessible to guest molecules, offering potential for stereoselective host−guest interactions. They are rare examples of coordination assemblies with built-in chiral functionalities with the potential for crystallographic studies of host−guest interactions and supramolecular chemistry.[11,12,18]

The coexistence of the ligands H_2L^1 and H_2L^0 in a 1:1 molar ratio in **2** was directly confirmed by single crystal X-ray diffraction of C═N and C−N bonds (Figure 1e and Figure S11), which was also proved by ^{1}H NMR after decomposition of the complex with aqueous hydrochloric acid (Figure S2−S4). X-ray photoelectron spectroscopy (XPS) showed that the content of C═N species[31] in high-resolution C 1s spectra is gradually increased with the increasement of salen ligand H_2L^0 from **1** to **3** (4.63%, 9.27%, and 14.55% for **1**, **2**, and **3**, respectively) (Figure 2h). On the other hand, the high-resolution N 1s spectra showed a gradually decrease of C−N species[31,32] (48.38%, 34.19%, and 6.47% for **1**, **2**, and **3**, respectively) and increase of C═N species (13.44%, 22.77%, and 45.67% for **1**, **2**, and **3**, respectively) (Figure 2i), the relative content of C−N/C═N is 3.60, 1.50, and 0.14 from **1** to **3**, respectively, which is in accord with the formation of metallacycles **1**−**3** by salalen (**1**, six H_2L^1), salalen/salen (**2**, three H_2L^1 and three H_2L^0), or salen (**3**, six H_2L^0). The formation of these metallacycles was also supported by ESI-MS (Figure S6, S8−S9).

Solid-state CD spectra of **1** and **2** constructed from (*R*)- and (*S*)-enantiomers of H_2L are mirror images of each other, indicating their enantiomeric relationship (Figure 2j). The optical band gaps (E_g) of **1**−**3** were estimated to be 2.84, 2.82, and 2.77 eV (Figure S16) from the electronic spectra and the relationship $[F(R)h\nu]^2 = h\nu - E_g$, where $h\nu$ is the corresponding phonon energy, and R is the diffuse reflectance.[33] These results indicate that **1**−**3** are a new type of semiconductor fluorescent metallacycle. The phase purity of the bulk samples was established by comparing the observed and simulated powder X-ray diffraction (PXRD) (Figure S19). PLATON calculations indicated the presence of 27.8% and 26.6% void space in **1** and **2**,[34] respectively. TGA revealed that the solvent molecules could be removed from **1** and **2** in the 80−150 °C range (Figure S20). PXRD experiments suggested that the samples retained their structural integrity and crystallinity upon removal of the guest molecules. Their permanent porosity was confirmed by their N_2 adsorption isotherms at 77 K. After desolvation, **1** and **2** exhibited a Type-I sorption behavior, with a BET surface area of 490 and 475 m^2 g^{-1}, respectively (Figure S21). Note that **3** has a BET surface area of 504 m^2 g^{-1}.[17]

Enantioselective Binding and Biosensing. Metallacycles **1**−**3** possess strong fluorescent in THF with an emission maximum around 465 nm. The presence of chiral cavities and NH groups in the metallacyclic compelxes **1**−**3** promoted the exploration of enantioselective recognition of important α-hydroxycarboxylic acids such as mandelic acid (MA) and sugar acids (Figure 3). When (*R*)-**1** was treated with enantio-pure MA (1.0×10^{-3} M), the UV−vis spectrum remained unchanged, indicative of the stability of the host structure (Figure S17). In contrast to the absorption spectrum, however, the emission was quenched, but the rate of change with L-MA was faster than that with D-MA (Figure S23). The intensity of (*R*)-**1** was maximally decreased to 62.3% and 83.2% of the original value by L- and D-MA, respectively. In accordance with the Stern−Völmer (S−V) equation, the measured absorbance I_0/I at 465 nm varied as a function of concentration (mM) in a linear relationship ($R^2 > 0.9900$), suggesting 1:1 stoichiometry of the interaction between MA and the host (*R*)-**1**.[35] The K_{sv} constants were calculated as 10059 ± 350 M^{-1} with L-MA and 3857 ± 80 M^{-1} with D-MA, giving an enantioselectivity factor $K_{sv(R\text{-}\mathbf{1}-L)}/K_{sv(R\text{-}\mathbf{1}-D)}$ of 2.61 ± 0.15 (Figure 3a). The opposite trend in selectivity was observed for quenching of (*S*)-**1** with L- and D-MA, for which the factor $K_{sv(S\text{-}\mathbf{1}-D)}/K_{sv(S\text{-}\mathbf{1}-L)}$ was 2.59 ± 0.12 (Figure S26), further confirming enantioselectivity in the fluorescent recognition. From control experiments, the free salalen ligand H_2L^1 did not show obvious enantioselectivity under otherwise identical conditions (Figure S27), suggesting a better-defined chiral environment conferred by the cyclic structure imposed by the metal coordination environment.

After titration with L-MA, the quantum yield (Φ_{fl}) of **1** decreased from 12.75% to 9.44%; the host−guest adducts of **1** and the MA analyte were also suggested by ESI-MS (Figure S7). The static nature of the complexation is suggested by consistent fluorescence lifetimes of the host before and after titration with L-MA (lifetime, τ_0, 2.908 vs 2.897 ns, Figure S28). Complex of the analyte with metallacycle **1** in the ground state via supramolecular interactions including hydrogen bonding followed by the generation of an emissive electron-transfer excited state or energy transfer may be responsible for the fluorescence change. Furthermore, the apparent quenching constant K_q ($K_q = K_{sv}/\tau_0$) for the metallacycles **1** with L-MA system is evaluated to be 3.46×10^{12} M^{-1} s^{-1}, which is even 2 orders of magnitude higher than that of conventional bimolecular diffusion based quenching mechanisms ($\sim 10^{10}$ M^{-1} s^{-1}).[36] In addition, exposure of (*R*)-**1** to MA (0.56 mM) with enantiomeric compositions ranging from −100 to 100% enantiomeric excess (ee) relative to the L enantiomer (Figure 3i) revealed that the quenching level (I_0/I) was linearly correlated with the ee of MA ($R^2 = 0.9971$). The ee values of MA samples thus can be rapidly determined by a simple fluorescence quenching measurement with **1**. This finding represents a significant step forward in the development of new generation chiral supramolecular sensors for applications.

The addition of enantiopure MA to solutions of (*R*)-**2** or (*R*)-**3** in THF also caused a decrease in the emission intensity, but with lower enantioselectivity. The $K_{sv(R\text{-}\mathbf{2}-L)}/K_{sv(R\text{-}\mathbf{2}-D)}$ ratio is 1.75 ± 0.13 and the $K_{sv(R\text{-}\mathbf{3}-L)}/K_{sv(R\text{-}\mathbf{3}-D)}$ is 1.24 ± 0.10 (Table S7, Figure S32−S33). The decrease in K_{sv} constants and enantioselectivity factors in the order **1** > **2** > **3** is consistent

DOI: 10.1021/jacs.6b11422
J. Am. Chem. Soc. 2017, 139, 1554−1564

Table 1. Stern–Völmer Binding Constant and Enantioselectivity Factor of (*R*)-1 and (*S*)-1 upon Titration with Different Sugar Acids and Amino Acids

entry	guest	$K_{sv(R)}$ [M^{-1}]	$K_{sv(S)}$ [M^{-1}]	$K_{sv(R)}/K_{sv(S)}$
1	D-glucuronic acid	4440 ± 150	16561 ± 700	1:3.73 ± 0.29
2	D-galacturonic acid	5534 ± 200	11721 ± 400	1:2.12 ± 0.15
3	D-gluconic acid	4587 ± 150	13040 ± 500	1:2.84 ± 0.21
4	D-glucaric acid	7596 ± 300	25338 ± 1100	1:3.34 ± 0.28
5	L-valine	21100 ± 850	4345 ± 150	4.86 ± 0.37:1
6	L-leucine	24627 ± 1000	8240 ± 300	2.99 ± 0.23:1
7	L-threonine	55627 ± 1650	21927 ± 950	2.54 ± 0.19:1
8	L-phenylalanine	41509 ± 1400	13173 ± 500	3.15 ± 0.24:1
9	L-tryptophan	30672 ± 1100	12482 ± 400	2.46 ± 0.17:1
10	L-dopa	78841 ± 2200	13032 ± 550	6.05 ± 0.44:1
11	D-penicillamine	85995 ± 2600	16318 ± 800	5.27 ± 0.43:1

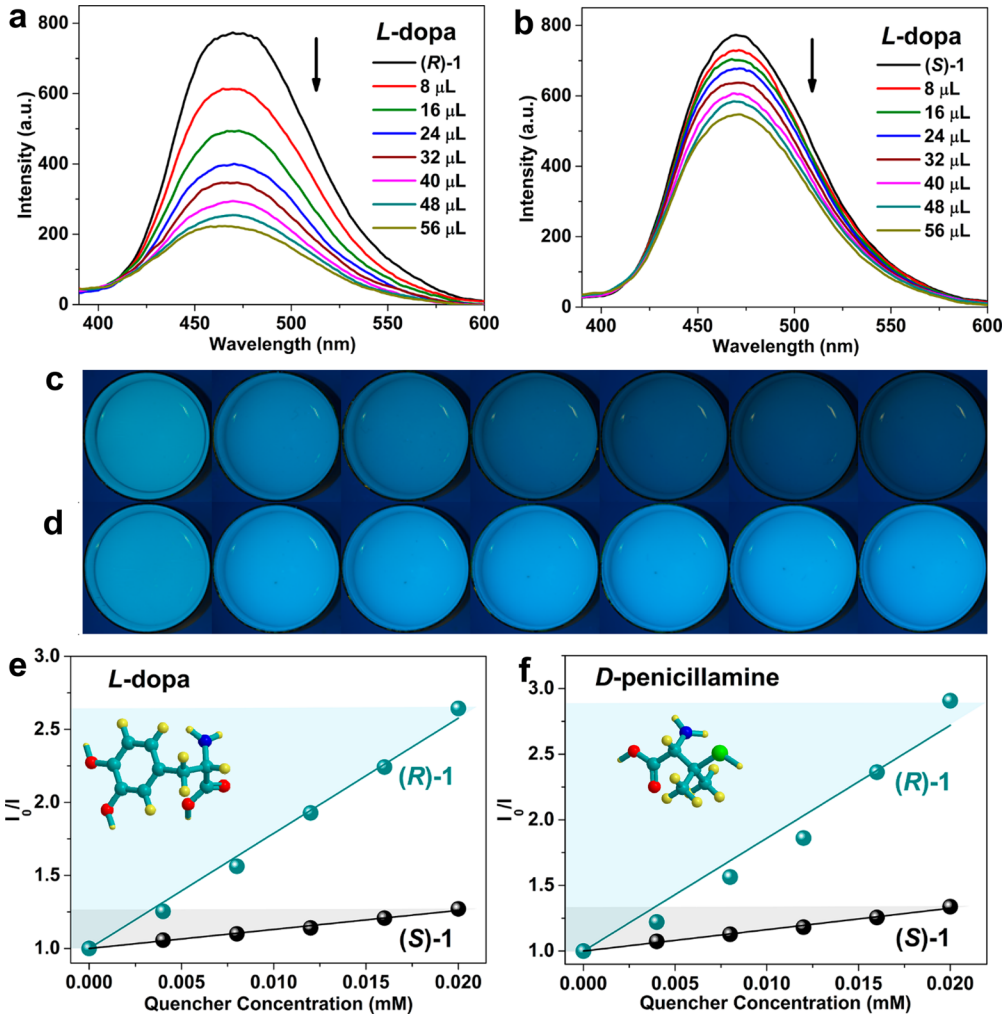

Figure 4. (a,b) Fluorescence emission spectra of (*R*)- and (*S*)-**1** (2.0×10^{-6} M in THF) upon titration with L-dopa ($c = 1 \times 10^{-3}$ M, λ_{ex} = 350 nm). Fluorescence photographs of (*R*)-**1** (c) and (*S*)-**1** (d) upon titration with L-dopa (0, 10, 20, 30, 40, 50, and 60 μL, respectively. λ_{ex} = 365 nm). (e,f) Stern–Völmer plots of (*R*)- and (*S*)-**1** titration with L-dopa and D-penicillamine (1×10^{-3} M).

with the total number of chiral NH groups within the cyclic structures, indicating the key role of these moieties in the recognition of chiral guests.

Interestingly, the metallacyclic system displayed enantioselective binding with a range of sugar acids, including D-glucuronic acid, D-galacturonic acid, D-gluconic acid, D-glucaric acid, and tartaric acid. The selectivity factors $K_{sv(S\text{-}1)}/K_{sv(R\text{-}1)}$ were determined as 3.73 ± 0.29, 2.12 ± 0.15, 2.84 ± 0.21, and 3.34 ± 0.28, respectively (Figure 3b–d and Table 1). Although **1** is enantioselective to tartaric acid, the S–V plot became nonlinear (Figure S34). Again, metallacycles **2** and **3** are also enantioselective to sugar acids. For example, the $K_{sv(S\text{-}2)}/K_{sv(R\text{-}2)}$ and $K_{sv(S\text{-}3)}/K_{sv(R3)}$ values with D-gluconic acid were found to be 2.00 ± 0.11 and 1.60 ± 0.09 (Table S8, Figure S39–S40), respectively, both of which are again smaller than that of **1** (3.73 ± 0.29). The enantioselectivity factors of **1** for D-

DOI: 10.1021/jacs.6b11422
J. Am. Chem. Soc. 2017, 139, 1554–1564

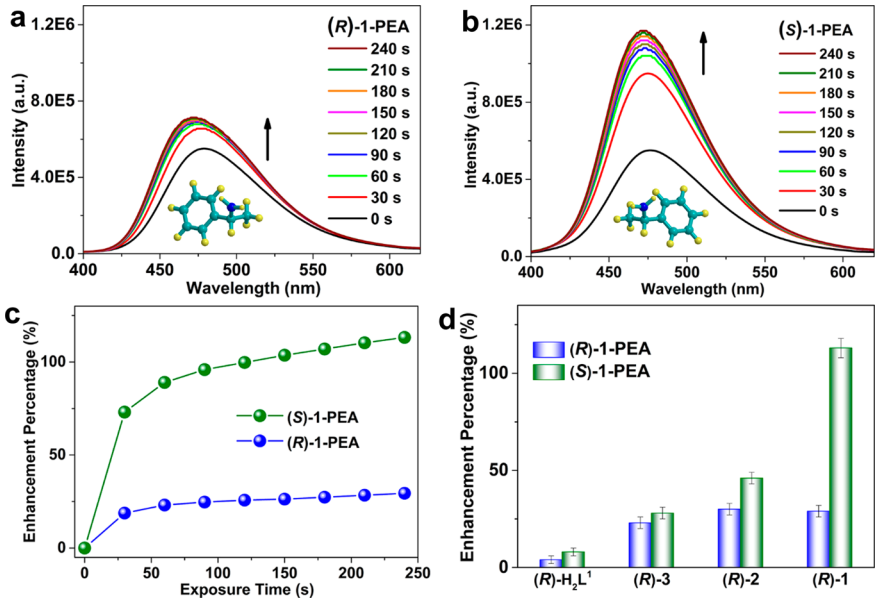

Figure 5. (a,b) Fluorescence enhancement upon the exposure of thin films of (*R*)-**1** to the saturated vapors of (*R*)- and (*S*)-1-PEA (λ_{ex} = 375 nm). (c) Time-dependent fluorescence enhancement of (*R*)-**1** by (*R*)- and (*S*)-1-PEA. (d) The compared enhancement percentages of (*R*)-H_2L^1, (*R*)-**1**, (*R*)-**2**, and (*R*)-**3** by (*R*)- and (*S*)-1-PEA after 4 min.

glucuronic acid and D-galacturonic acid are obviously larger than the well-known sensors of bisbinaphthyl biboronic acids for sugar acids (3.7 vs 2.0 and 2.1 vs 1.2),[37] whereas the values of D-gluconic acid and D-glucaric acid are comparable with those of the boronic acid system.

Metallacycle **1** is also stable and highly enantioselective toward a variety of amino acids (Figure S17). When **1** was treated with L-valine, L-leucine, L-threonine, L-phenylalanine, and L-tryptophan (1.0×10^{-3} M), respectively, the decreased rates of fluorescence for (*R*)-**1** were faster than those of (*S*)-**1**. The $K_{sv(R\text{-}1)}/K_{sv(S\text{-}1)}$ values were calculated as 4.86 ± 0.37, 2.99 ± 0.23, 2.54 ± 0.19, 3.15 ± 0.24, and 2.46 ± 0.17 (Figure 3e–h and Table 1), respectively. Although many synthetic receptors for enantioselective recognition of amino acids have been synthesized, no assembled receptors have been reported to exhibit such high enantioselectivity.[11,12,38−40] Again, **1** also showed higher enantioselectivity toward amino acids than **2** and **3**. For example, the enantioselectivity factor $K_{sv(R\text{-}2)}/K_{sv(S\text{-}2)}$ and $K_{sv(R\text{-}3)}/K_{sv(S\text{-}3)}$ with L-phenylalanine were 1.58 ± 0.09 and 1.05 ± 0.06 for **2** and **3** (Table S9, Figure S48–S49), respectively, which are much smaller than the value of 3.15 ± 0.24 for **1**.

More importantly, metallacycle **1** could also detect chiral drugs such as L-dopa (a drug for Parkinson's disease) and D-penicillamine (a drug for rheumatoid arthritis and chronic active hepatitis). Obviously, the rates of fluorescence decrease of (*R*)-**1** caused by L-dopa and D-penicillamine were faster than those of (*S*)-**1** (Figure 4a,b). The constants $K_{sv(R\text{-}1)}$ of D-penicillamine and L-dopa are up to 85995 ± 2600 and 78841 ± 2200 M^{-1} (Table 1), respectively; the $K_{sv(R\text{-}1)}/K_{sv(S\text{-}1)}$ ratios with L-dopa and D-penicillamine are 6.05 ± 0.44 and 5.27 ± 0.43 (Figure 4e,f), respectively. Fluorescence photographs also clearly showed that (*R*)-**1** was quenched more quickly than (*S*)-**1** upon titration with L-dopa (Figure 4c,d). The detection limits ($3\sigma/K_{sv}$, σ is standard deviation of this detection method) of L-dopa and D-penicillamine are calculated to be 5.46×10^{-4} and 5.01×10^{-4} M, respectively. The low detection concentration and the high quenching constant for L-dopa and D-penicillamine drugs reveal that **1** is an excellent chiral biosensor for sensitive and selective detection of bioactive molecules. To the best of our knowledge, this is the first example of enantioselective biosensing of L-dopa and D-penicillamine chiral drugs with high quenching constants and enantioselectivity factors. Given that the detection of these chiral drug analytes can be done immediately upon mixing with **1** without any extra sample treatment, such processes may be a useful path toward medical drug monitoring.

Enantioselective Gas Sensing of Chiral Amines. Chiral discrimination of amine vapors plays an important role in olfactory perception of biological systems,[41] and the mimicry of such systems for sensing odors through the development of "artificial noses" is an area of considerable interest.[42,43] The fluorescence spectra of metallacycles **1** in thin layer forms were monitored upon exposure to the saturated vapor of chiral amines for varied and specified periods of time.[12,44] When (*R*)-**1** was exposed to the 1-phenylethylamine (1-PEA) vapor, the emission at 475 nm was shifted to 465 nm and enhanced by both the *R* and *S* enantiomers, but the rate caused by (*S*)-1-PEA was much faster than that by the (*R*)-enantiomer (Figure 5a,b). The enhancement percentages of (*R*)- and (*S*)-1-PEA were 29% and 113% after 240 s, with the I/I_0 ratios of 1.29 and 2.13 (Figure 5c), respectively. The enantioselectivity factor [ef = $(I_S/I_0 - 1)/(I_R/I_0 - 1)$][12] was determined as 3.90 ± 0.52. Time-resolved fluorescence measurements of (*R*)-**1** after addition of (*S*)-1-PEA showed only a slight change in decay rate, the fluorescence lifetimes (τ_0, 1.480 vs 2.350 ns) remained almost unchanged (Figure S50), and PXRD measurement indicated that **1** remained highly crystalline after exposure to (*S*)-1-PEA saturated vapors (Figure S19). All these are indicative of the stability of the host. The sensing had short times and might be well-suited to perform a quick analysis of enantiomers of secondary amines and their derivatives.

Control experiments indicated that the solid (*R*)-H_2L^1 ligands showed almost no fluorescence change with (*S*)- or (*R*)-1-PEA and no enantioselectivity (Figure S51). Note that, under otherwise identical conditions, the I/I_0 ratio of (*R*)-**2** and

DOI: 10.1021/jacs.6b11422
J. Am. Chem. Soc. 2017, 139, 1554−1564

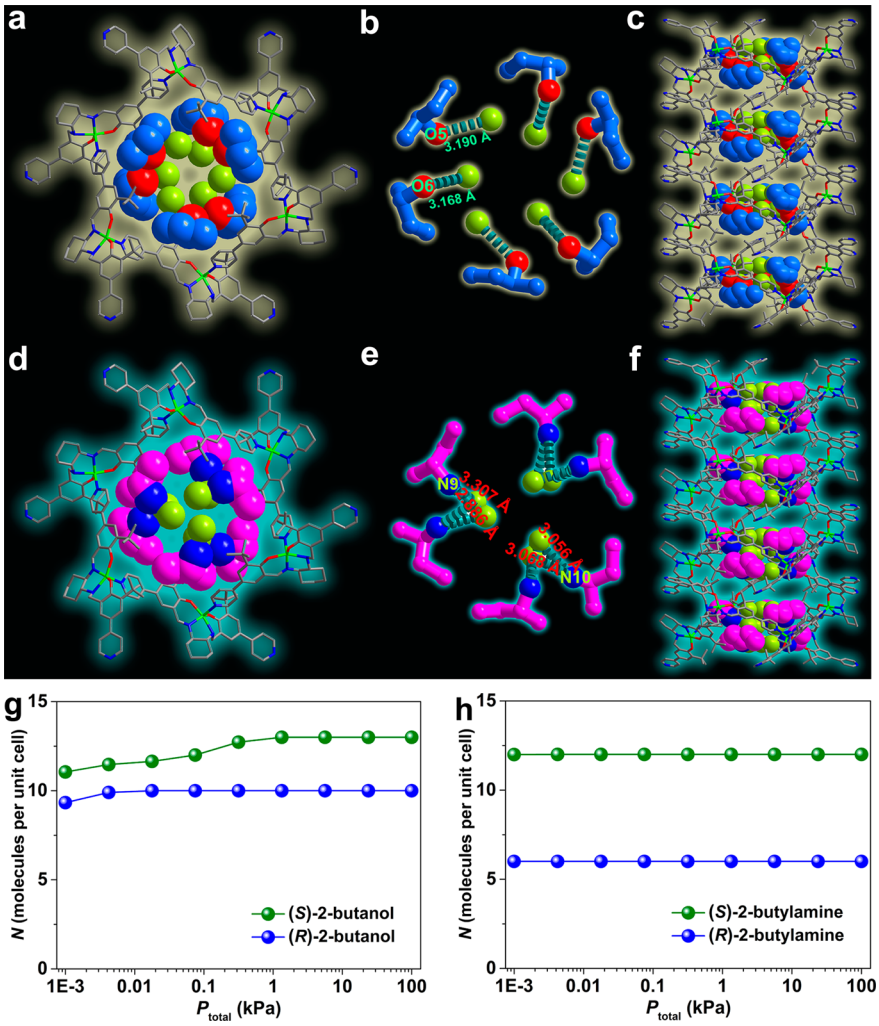

Figure 6. X-ray crystal structures of 6(*S*)-2-butanol·6H_2O (a) and 6(*S*)-2-butylamine·9H_2O (d) adsorbed in the chiral pocket of (*R*)-**1**. Hexamer of six (*S*)-2-butanol (b) and (*S*)-2-butylamine (e) with water molecules through hydrogen bonds in a slipped parallel conformation in the chiral pocket. The side view of 6(*S*)-2-butanol·6H_2O (c) and 6(*S*)-2-butylamine·9H_2O (f) adsorbed in the chiral pocket, which generated nanotubes through strong supramolecular interactions. Color coding: Zn; green, O; red, N; blue, C is gray in (*R*)-**1**. (*S*)-2-butanol and (*S*)-2-butylamine molecules using space-filling model are colored as follows: (*S*)-2-butanol C, blue; O, red; Water, green. (*S*)-2-butylamine C, purple; O, blue; Water green. Adsorption isotherms of racemic mixtures in (*R*)-**1**: (*S*)-/(*R*)-2-butanol (g) and (*S*)-/(*R*)-2-butylamine (h) from molecular simulations.

(*R*)-**3** was increased to 1.46, 1.30, 1.28, and 1.23 by (*S*)- and (*R*)-1-PEA, with an ef of 1.53 ± 0.23 and 1.22 ± 0.18 for (*R*)-**2** and (*R*)-**3** (Figure S52–S53), respectively, smaller than that observed for (*R*)-**1** (3.90 ± 0.52) (Figure 5d). This experimental result again illustrates the key role of chiral NH functionalities in the enantioselective gas sensing. Significant enantioselective fluorescence enhancements of (*R*)-**1** with other chiral amines such as 1-phenylpropylamine (1-PPA) and 1,2-cyclohexanediamine (CDA) were also observed. In both cases, the rate of increase caused by the (*S*)-enantiomer was also faster than that caused by the (*R*)-enantiomer (Figure S54–S55). The ef values by (*R*)-**1** were calculated as 1.80 ± 0.22 and 2.70 ± 0.35 for 1-PPA and CDA, respectively. The enantioselectivity decreased in the order 1-PEA > CDA > 1-PPA.

Single-Crystal X-ray Diffraction Analyses of the Host–Guest Adducts. Although it was not possible to obtain single-crystal structures of **1** containing encapsulated sugar acids, amino acid, or 1-PEA, crystals suitable for X-ray analysis were obtained from crystallization of (*R*)-**1** with racemic 2-butylamine or 2-butanol. The X-ray single-crystal structures indicated that (*R*)-**1** trapped (*S*)-2-butanol and (*S*)-2-butylamine from the racemic mixture to form [(*R*)-**1**·6(*S*)-2-butanol·6H_2O] and [(*R*)-**1**·6(*S*)-2-butylamine·9H_2O] (Figure 6a–d), respectively. The desorbed guest molecules from (*R*)-**1** were analyzed by using HPLC on a chiral support, which showed that the enantiomeric excess value was 99.4% for (*S*)-2-butylamine and 97.5% for (*S*)-2-butanol (Figure S56), respectively, In fact, **1** is among the best porous materials for enantioseparation of 2-butanol[17,18] and is superior to our best demonstrated metal–organic frameworks (MOFs) for 2-butylamine (99.4% vs 82% ee).[45]

As shown in Figure 6, six (*S*)-2-butanol or (*S*)-2-butylamine molecules are trapped in six pockets of the metallacycles and each of them is involved with different supramolecular interactions: hydrogen bonds with cocrystallized water molecules through its amine or hydroxyl group (N···O = 2.886–3.068 Å, and O···O = 3.168–3.190 Å) and hydrophobic interactions with metallosalalen units through its methyl and ethyl groups, respectively. Notably, there are three pairs of six or nine water molecules in the macrocycle cavity, which are related by 3-fold symmetry and form a distorted trigonal prism-

DOI: 10.1021/jacs.6b11422
J. Am. Chem. Soc. 2017, 139, 1554–1564

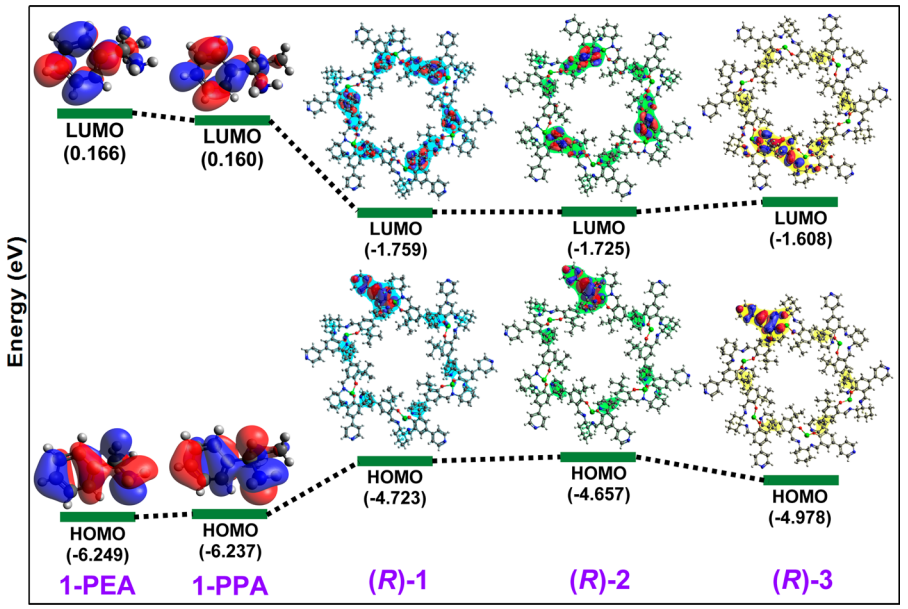

Figure 7. HOMO−LUMO energy profiles of 1-PEA, 1-PPA, (*R*)-**1**, (*R*)-**2**, and (*R*)-**3** in vacuum.

shaped structure. Although the chiral NH groups of the salalen ZnL^1 complexes are not directly engaged in supramolecular interactions with guest molecules, they, together with the Zn atoms and phenyl rings, create a chiral microenvironment in the metallacycle. In this way, the host transfers its chirality to the structural organization of the water and organic molecules. Therefore, the specific recognition of **1** for enantiomers of secondary amines and alcohols is attributed to the confinement of the chiral pockets induced by chiral Zn(salalen) units, additionally it is enhanced by the supramolecular interactions between host and guest molecules.

Molecular Simulations. To microscopically elucidate the observed enantioselective adsorption of 2-butanol and 2-butylamine in (*R*)-**1**, molecular simulations were conducted (Figures S57−S60). The binding energies of a single (*S*)- and (*R*)-2-butanol molecule with (*R*)-**1** are −76.59 ± 4.63 and −70.22 ± 5.58 kJ mol^{-1}, respectively. As for a single (*S*)- and (*R*)-2-butylamine molecule, the binding energies are −74.41 ± 1.75 and −71.71 ± 1.20 kJ mol^{-1}, respectively. This indicates that the (*S*)-enantiomers of 2-butanol and 2-butylamine have stronger interactions than their (*R*)-counterparts with (*R*)-**1**. The adsorption isotherms of racemic mixtures of (*S*)-/(*R*)-2-butanol and (*S*)-/(*R*)-2-butylamine in (*R*)-**1** are shown in Figures 6g,h. The difference in binding energies is then responsible for the enantioselective adsorption.[46,47]

Density Functional Theory Calculations. Density functional theory (DFT) calculations were conducted on metallacyclic hosts and typical analytes to better understand the different fluorescence emissions of metallacycles in the presence of various analytes such as amines (turn-on) or sugar acids and amino acids (turn-off). Based on the results of DFT calculations (Figure 7), the energies of the lowest unoccupied molecular orbitals (LUMO) of (*R*)-**1** (−1.759 eV), (*R*)-**2** (−1.725 eV), and (*R*)-**3** (−1.608 eV) are below the LUMO energies of 1-PEA (0.166 eV) and 1-PPA (0.160 eV), which allows an efficient electron transfer from 1-PEA and 1-PPA to metallacycle **1**−**3** resulting in fluorescence enhancement (donor−acceptor electron-transfer mechanism[44,48]). This was also observed in other porous materials such as porous organic frameworks (POFs),[49] covalent organic frameworks (COFs),[50] and MOFs.[44,51] In the case of fluorescence quenching by L-dopa, D-glucuronic acid, and L-MA in THF, although the calculated DFT results do not follow an electron-transfer mechanism (Figures S61−S62), the energy transfer contributes significantly in fluorescence quenching and should also be considered. The electronic absorption spectra show that all these guests absorb excitation energy used in the sensing experiment (Figure S63−S64). This suggests that competition between the metallacyclic hosts and the sugar acids or amino acids guests for excitation energy may also contribute to the quenching of emission from the metallacycles. Similar phenomena were also observed in luminescent MOFs.[51]

As above-mentioned, the enantioselectivity in fluorescence response may result from the formation of different diastereomeric complexes. Single-crystal diffraction, molecular simulations, and DFT calculations indicated that the (*S*)-enantiomers of the analytes would be bound to (*R*)-**1** more strongly than (*R*)-enantiomers. As a consequence, the rates of energy transfer from (*R*)-**1** to the (*S*)-enantiomers of α-hydroxycarboxylic acids and amino acids are faster than those to the (*R*)-enantiomers, leading to enantioselective fluorescence quenching. In contrast, the rates of electron transfer of from (*S*)-1-PEA to (*R*)-**1** was faster than that to the (*R*)-enantiomer, giving rise to enantioselective fluorescence enhancement. Notably, the strength of host−guest interactions is greatly influenced by the number of chiral NH groups within the metallacycle structure, and so the selectivity and affinity of metallacycles **1**−**3** to the analytes decrease in the order **1** > **2** > **3**.

■ CONCLUSIONS

In summary, the endogenous precisely adjusted self-assembly approach presented here opens a new avenue for constructing novel chiral NH-controlled supramolecular metallacycles with high-affinity and -enantioselectivity binding of biologically active molecules. The assembly of metallosalalens and metallosalens affords chiral fluorescent Zn_6L_6 metallacycles **1**−**3** bearing six, three, and zero NH groups that could be packed through strong supramolecular interactions to generate porous

DOI: 10.1021/jacs.6b11422
J. Am. Chem. Soc. 2017, 139, 1554−1564

architectures with permanent porosity. The metallacycles are capable of enantioselective discrimination of the enantiomers of sugar acids and amino acids through fluorescence quenching in solution and the enantiomers of 1-PEA through fluorescence enhancement in a crystalline state. The selectivity and binding affinity are greatly affected by the available NH groups in the metallacycles, which decrease significantly from **1** to **2** and to **3**. From single-crystal X-ray diffraction, molecular simulations, and DFT calculations, the intrinsic chiral recognition and discrimination are attributed to the specific binding of enantiomers in the chiral microenvironment of the crystalline metallacycles. The enantioselective fluorescence change was also explained by the donor−acceptor electron-transfer mechanism. Manipulation of chiral NH functionalities in metallacycles can control the enantiorecognition of biomolecular complexes, which may provide new opportunities for the assembly of more effective chiral supramolecular materials for enantioselective processes.

■ ASSOCIATED CONTENT

Supporting Information

The Supporting Information is available free of charge on the ACS Publications website at DOI: 10.1021/jacs.6b11422.

Experimental details on synthesis and characterization of salalen ligands H_2L_1 and metallacycles **1**−**3**, fluorescence sensing of α-hydroxycarboxylic acids, amino acids and chiral amines, molecular simulations and DFT calculations (PDF)

Crystallographic information files (CIF) for (*R*)-**1**, (*R*)-**2**, (*R*)-**1**−2-butanol, and (*R*)-**1**−2-butylamine (ZIP)

■ AUTHOR INFORMATION

Corresponding Authors

*yongcui@sjtu.edu.cn

*liuy@sjtu.edu.cn

ORCID

Paul J. Low: 0000-0003-1136-2296

Jianwen Jiang: 0000-0003-1310-9024

Yong Cui: 0000-0003-1977-0470

Notes

The authors declare no competing financial interest.

■ ACKNOWLEDGMENTS

We gratefully acknowledge the financial support of the NSFC (Grants 21371119, 21431004, 21401128, 21522104, and 21620102001), the "973" Program (Grants 2014CB932102, 2012CB8217, and 2016YFA0203400), SSTC-12XD1406300, and the "Eastern Scholar" Program, the National University of Singapore, and the Ministry of Education of Singapore (Grants R-279-000-474-112 and R-279-000-437-112).

■ REFERENCES

(1) Stymiest, J. L.; Bagutski, V.; French, R. M.; Aggarwal, V. K. *Nature* **2008**, *456*, 778−782.

(2) Zhang, X.; Yin, J.; Yoon, J. *Chem. Rev.* **2014**, *114*, 4918−4959.

(3) Roth, J. *Chem. Rev.* **2002**, *102*, 285−304.

(4) Mooibroek, T. J.; Casas-Solvas, J. M.; Harniman, R. L.; Renney, C. M.; Carter, T. S.; Crump, M. P.; Davis, A. P. *Nat. Chem.* **2016**, *8*, 69−74.

(5) Sookcharoenpinyo, B.; Klein, E.; Ferrand, Y.; Walker, D. B.; Brotherhood, P. R.; Ke, C.; Crump, M. P.; Davis, A. P. *Angew. Chem., Int. Ed.* **2012**, *51*, 4586−4590.

(6) Destecroix, H.; Renney, C. M.; Mooibroek, T. J.; Carter, T. S.; Stewart, P. F. N.; Crump, M. P.; Davis, A. P. *Angew. Chem., Int. Ed.* **2015**, *54*, 2057−2061.

(7) Ke, C.; Destecroix, H.; Crump, M. P.; Davis, A. P. *Nat. Chem.* **2012**, *4*, 718−723.

(8) Rios, P.; Carter, T. S.; Mooibroek, T. J.; Crump, M. P.; Lisbjerg, M.; Pittelkow, M.; Supekar, N. T.; Boons, G.-J.; Davis, A. P. *Angew. Chem., Int. Ed.* **2016**, *55*, 3387−3392.

(9) Yan, X.; Cook, T. R.; Pollock, J. B.; Wei, P.; Zhang, Y.; Yu, Y.; Huang, F.; Stang, P. J. *J. Am. Chem. Soc.* **2014**, *136*, 4460−4463.

(10) Chi, X.; Ji, X.; Xia, D.; Huang, F. *J. Am. Chem. Soc.* **2015**, *137*, 1440−1443.

(11) Xuan, W.; Zhang, M.; Liu, Y.; Chen, Z.; Cui, Y. *J. Am. Chem. Soc.* **2012**, *134*, 6904−6907.

(12) Dong, J.; Zhou, Y.; Zhang, F.; Cui, Y. *Chem. - Eur. J.* **2014**, *20*, 6455−6461.

(13) Cook, T. R.; Zheng, Y.-R.; Stang, P. J. *Chem. Rev.* **2013**, *113*, 734−777.

(14) Cook, T. R.; Stang, P. J. *Chem. Rev.* **2015**, *115*, 7001−7045.

(15) Lee, S. J.; Lin, W. *Acc. Chem. Res.* **2008**, *41*, 521−537.

(16) Liu, Y.; Xuan, W.; Cui, Y. *Adv. Mater.* **2010**, *22*, 4112−4135.

(17) Li, G.; Yu, W.; Cui, Y. *J. Am. Chem. Soc.* **2008**, *130*, 4582−4583.

(18) Liu, T.; Liu, Y.; Xuan, W.; Cui, Y. *Angew. Chem., Int. Ed.* **2010**, *49*, 4121−4124.

(19) Wu, K.; Li, K.; Hou, Y.-J.; Pan, M.; Zhang, L.-Y.; Chen, L.; Su, C.-Y. *Nat. Commun.* **2016**, *7*, 10487.

(20) Chen, S.; Li, K.; Zhao, F.; Zhang, L.; Pan, M.; Fan, Y.-Z.; Guo, J.; Shi, J.; Su, C.-Y. *Nat. Commun.* **2016**, *7*, 13169.

(21) Zhao, C.; Sun, Q.-F.; Hart-Cooper, W. M.; DiPasquale, A. G.; Toste, F. D.; Bergman, R. G.; Raymond, K. N. *J. Am. Chem. Soc.* **2013**, *135*, 18802−18805.

(22) Kaphan, D. M.; Toste, F. D.; Bergman, R. G.; Raymond, K. N. *J. Am. Chem. Soc.* **2015**, *137*, 9202−9205.

(23) Saha, M. L.; Yan, X.; Stang, P. J. *Acc. Chem. Res.* **2016**, *49*, 2527−2539.

(24) Yan, X.; Cook, T. R.; Wang, P.; Huang, F.; Stang, P. J. *Nat. Chem.* **2015**, *7*, 342−348.

(25) Yan, X.; Wang, H.; Hauke, C. E.; Cook, T. R.; Wang, M.; Saha, M. L.; Zhou, Z.; Zhang, M.; Li, X.; Huang, F.; Stang, P. J. *J. Am. Chem. Soc.* **2015**, *137*, 15276−15286.

(26) Yan, X.; Wang, M.; Cook, T. R.; Zhang, M.; Saha, M. L.; Zhou, Z.; Li, X.; Huang, F.; Stang, P. J. *J. Am. Chem. Soc.* **2016**, *138*, 4580−4588.

(27) Tian, Y.; Yan, X.; Saha, M. L.; Niu, Z.; Stang, P. J. *J. Am. Chem. Soc.* **2016**, *138*, 12033−12036.

(28) Ye, Y.; Cook, T. R.; Wang, S.-P.; Wu, J.; Li, S.; Stang, P. J. *J. Am. Chem. Soc.* **2015**, *137*, 11896−11899.

(29) Matsumoto, K.; Saito, B.; Katsuki, T. *Chem. Commun.* **2007**, 3619−3627.

(30) Morris, G. A.; Zhou, H.; Stern, C. L.; Nguyen, S. T. *Inorg. Chem.* **2001**, *40*, 3222−3227.

(31) Sheng, Z.-H.; Shao, L.; Chen, J.-J.; Bao, W.-J.; Wang, F.-B.; Xia, X.-H. *ACS Nano* **2011**, *5*, 4350−4358.

(32) Ci, L.; Song, L.; Jin, C.; Jariwala, D.; Wu, D.; Li, Y.; Srivastava, A.; Wang, Z. F.; Storr, K.; Balicas, L.; Liu, F.; Ajayan, P. M. *Nat. Mater.* **2010**, *9*, 430−435.

(33) Tai, G.; Hu, T.; Zhou, Y.; Wang, X.; Kong, J.; Zeng, T.; You, Y.; Wang, Q. *Angew. Chem., Int. Ed.* **2015**, *54*, 15473−15477.

(34) Spek, A. *J. Appl. Crystallogr.* **2003**, *36*, 7−13.

(35) Mei, X.; Wolf, C. *J. Am. Chem. Soc.* **2004**, *126*, 14736−14737.

(36) Dalapati, S.; Jin, S.; Gao, J.; Xu, Y.; Nagai, A.; Jiang, D. *J. Am. Chem. Soc.* **2013**, *135*, 17310−17313.

(37) Zhao, J.; Davidson, M. G.; Mahon, M. F.; Kociok-Köhn, G.; James, T. D. *J. Am. Chem. Soc.* **2004**, *126*, 16179−16186.

(38) Ryu, D.; Park, E.; Kim, D.-S.; Yan, S.; Lee, J. Y.; Chang, B.-Y.; Ahn, K. H. *J. Am. Chem. Soc.* **2008**, *130*, 2394−2395.

(39) Soloshonok, V. A.; Ellis, T. K.; Ueki, H.; Ono, T. *J. Am. Chem. Soc.* **2009**, *131*, 7208−7209.

DOI: 10.1021/jacs.6b11422
J. Am. Chem. Soc. 2017, 139, 1554−1564

(40) Wanderley, M. M.; Wang, C.; Wu, C.-D.; Lin, W. *J. Am. Chem. Soc.* **2012**, *134*, 9050−9053.
(41) Islam, M. R.; Mahdi, J. G.; Bowen, I. D. *Drug Saf.* **1997**, *17*, 149−165.
(42) Bodenhofer, K.; Hierlemann, A.; Seemann, J.; Gauglitz, G.; Koppenhoefer, B.; Gpel, W. *Nature* **1997**, *387*, 577−580.
(43) Torsi, L.; Farinola, G. M.; Marinelli, F.; Tanese, M. C.; Omar, O. H.; Valli, L.; Babudri, F.; Palmisano, F.; Zambonin, P. G.; Naso, F. *Nat. Mater.* **2008**, *7*, 412−417.
(44) Pramanik, S.; Zheng, C.; Zhang, X.; Emge, T. J.; Li, J. *J. Am. Chem. Soc.* **2011**, *133*, 4153−4155.
(45) Peng, Y.; Gong, T.; Zhang, K.; Lin, X.; Liu, Y.; Jiang, J.; Cui, Y. *Nat. Commun.* **2014**, *5*, 4406.
(46) Wang, W.; Dong, X.; Nan, J.; Jin, W.; Hu, Z.; Chen, Y.; Jiang, J. *Chem. Commun.* **2012**, *48*, 7022−7024.
(47) Zhang, L.; Jiang, J. *J. Membr. Sci.* **2011**, *367*, 63−70.
(48) Thomas, S. W.; Joly, G. D.; Swager, T. M. *Chem. Rev.* **2007**, *107*, 1339−1386.
(49) Dong, J.; Tummanapelli, A. K.; Li, X.; Ying, S.; Hirao, H.; Zhao, D. *Chem. Mater.* **2016**, *28*, 7889−7897.
(50) Das, G.; Biswal, B. P.; Kandambeth, S.; Venkatesh, V.; Kaur, G.; Addicoat, M.; Heine, T.; Verma, S.; Banerjee, R. *Chem. Sci.* **2015**, *6*, 3931−3939.
(51) Hu, Z.; Lustig, W. P.; Zhang, J.; Zheng, C.; Wang, H.; Teat, S. J.; Gong, Q.; Rudd, N. D.; Li, J. *J. Am. Chem. Soc.* **2015**, *137*, 16209−16215.

DOI: 10.1021/jacs.6b11422
J. Am. Chem. Soc. 2017, 139, 1554−1564